

See discussions, stats, and author profiles for this publication at: <https://www.researchgate.net/publication/3173297>

Universal Induction Motor Model With Low-to-High Frequency-Response Characteristics

Article in *IEEE Transactions on Industry Applications* · October 2007

DOI: 10.1109/TIA.2007.904401 · Source: IEEE Xplore

CITATIONS
194

READS
8,923

5 authors, including:

 **Behrooz Mirafzal**
Kansas State University
154 PUBLICATIONS 4,397 CITATIONS
[SEE PROFILE](#)

 **Gary Leonard Skibinski**
Rockwell Automation
92 PUBLICATIONS 5,861 CITATIONS
[SEE PROFILE](#)

 **Rangarajan Tallam**
Rockwell Automation
62 PUBLICATIONS 2,926 CITATIONS
[SEE PROFILE](#)

 **Dave Schlegel**
Rockwell Automation
34 PUBLICATIONS 3,568 CITATIONS
[SEE PROFILE](#)

Universal Induction Motor Model With Low-to-High Frequency-Response Characteristics

Behrooz Mirafzal, *Member, IEEE*, Gary L. Skibinski, Rangarajan M. Tallam, *Senior Member, IEEE*, David W. Schlegel, *Member, IEEE*, and Richard A. Lukaszewski, *Senior Member, IEEE*

Abstract—A three-phase induction motor model that depicts the motor behavior over a wide range of frequencies from 10 Hz to 10 MHz is presented in this paper. The model is universal in the sense that common-mode, differential-mode, and bearing circuit models are combined into one three-phase equivalent circuit model. The proposed model is basically an extension of the low-frequency IEEE Standard 112 circuit model. The proposed model was experimentally simulated and verified with results presented.

Index Terms—Bearing current, common mode (CM), differential mode (DM), electromagnetic interference (EMI), high-frequency model, induction motor, pulsewidth-modulated (PWM) voltage source inverter, reflected wave, transient overvoltage.

I. INTRODUCTION

INDUSTRIAL applications of adjustable-speed drives (ASDs) using pulsewidth-modulated (PWM) voltage-source inverters with steep voltage pulse rise times (t_r) have been common place since 1980. What has evolved are more sophisticated three-phase control algorithms, along with power devices having faster rise times (< 100 ns) allowing higher control bandwidth and reducing inverter switching losses and magnetic filter volume, and faster switching cycles (4–20 kHz) to reduce motor current ripple harmonics, torque ripple, and acoustical noise, which consequently improve system performance. However, the fast rise time of the voltage transition also excites undesirable system secondary parasitic effects, such as reflected wave differential overvoltage spikes on motor terminals that reduce the motor insulation life, common-mode (CM) current that creates system electromagnetic interference (EMI) issues, and motor-bearing currents that drastically reduce the operating life [1].

A single inverter switching event may produce motor transients up to twice the dc-bus voltage due to mismatch between the cable characteristic impedance and the motor surge impedance, which leads to reflected waves [1]–[3]. Critical cable lengths at which the theoretical twice voltage magnitude

Paper IPCSD-07-023, presented at the 2006 Industry Applications Society Annual Meeting, Tampa, FL, October 8–12, and approved for publication in the IEEE TRANSACTIONS ON INDUSTRY APPLICATIONS by the Electric Machines Committee of the IEEE Industry Applications Society. Manuscript submitted for review October 31, 2006 and released for publication April 26, 2007.

The authors are with the Allen-Bradley Drives Division, Rockwell Automation, Mequon, WI 53092 USA (e-mail: bmirafzal@ra.rockwell.com; gskibinski@ra.rockwell.com; rmtallam@ra.rockwell.com; dwschlegel@ra.rockwell.com; ralukaszewski@ra.rockwell.com).

Color versions of one or more of the figures in this paper are available online at <http://ieeexplore.ieee.org>.

Digital Object Identifier 10.1109/TIA.2007.904401

occurs also depends on pulse rise time. ASDs using gate turnoff thyristor ($t_r = 2$ μ s), bipolar junction transistor ($t_r = 0.25$ –1 μ s), and the latest insulated-gate bipolar transistor (IGBT, $t_r = 0.05$ –0.25 μ s) devices have corresponding critical cable lengths of 300 m (\sim 1000 ft), 150 m (\sim 500 ft), and less than 15 m (\sim 50 ft). A faster IGBT rise time, along with high peak voltages in most applications, creates a nonlinear voltage gradient on the first turn and first coil of the stator winding [4], [5]. Internal winding voltages may exceed the insulation capability, which leads to interturn short circuit failure and subsequently to phase-to-phase or phase-to-ground catastrophic faults [6], [7].

Accurate simulation of the motor line-to-line overvoltage requires a distributed parameter transmission line rather than a lumped parameter model for the cable [8]–[11]. If inverter output filters are used, then simple R – L motor models may be adequate [12]; however, these motor models are unable to capture the high-frequency content present in the PWM voltage pulse on unfiltered outputs. Initially, only single transmission line cable simulation models were available, which limits the high-frequency differential-mode (DM) motor models that matched the induction motor transfer function to also be single line based [9], [13], [14]. These models matched the motor line-to-line impedance transfer function with a low-frequency R – L circuit below the first resonance and a parallel R – C branch for higher frequency content to sufficiently predict the motor overvoltage waveform. Improvements in single-line models were made with the addition of CM and DM impedances in parallel with the machine d – q low-frequency model [15], [16]. One disadvantage of impedance matching schemes on single-line models is that the resulting elements have no direct correlation to machine geometry or known low-frequency motor parameters.

Recently, three-phase transmission line models [17] have become available, so a full three-phase simulation using a three-phase motor model with accurate low-to-high frequency response content is now possible. Three-phase PWM modulators can interact with cable and motor models, which create up to three times the bus voltage at the motor terminals, depending on the dwell time spacing between line-to-line voltage pulses [18]. The dwell time must be estimated offline before a single-line model can be used. Thus, it is advantageous to simulate a three-phase modulator that directly interacts with three-phase cable and motor circuits for any inverter operating point. Various three-phase control algorithms such as PWM sine triangle, sine triangle with third harmonic, space vector, and two-phase modulation can then be studied for instantaneous line-to-line

TABLE I
5-, 20-, AND 100-hp INDUCTION MOTORS' DESIGN SPECIFICS

MOTOR DIAMETERS	5 HP	20 HP	100 HP
Stator winding connections	Y	Δ	Δ
Number of parallel circuits	1	1	2
Stack length (mm)	114.3	158.8	203.2
Number of stator slots	36	48	60
Stator slot width (mm)	6.96	7.37	9.80
Stator slot depth (mm)	18.67	26.92	35.56

TABLE II
5-, 20-, AND 100-hp INDUCTION MOTORS' PARAMETERS
PER PHASE AT POWER FREQUENCY (60 Hz)

MOTOR PARAMETERS	5 HP	20 HP	100 HP
R_s (Ω)	1.410	0.267	0.030
R_r (Ω)	1.280	0.248	0.023
L_{ls} (mH)	11.350	2.910	0.653
L_{lr} (mH)	15.040	4.290	0.802
L_m (mH)	319	77.3	20.2
R_{core} (Ω)	2568	990	326

and line-to-ground waveform simulations. Lastly, use of active front-end converters with its switching action nonsynchronized with the inverter makes single-line models less accurate for determining the line-to-line and line-to-ground voltage stress on long cables [19]. Thus, a three-phase universal motor model is required.

Network simulation and modeling have become more important for EMI evaluation to existing International Electrotechnical Commission standards [20]. Implementing three-phase motor and cable models that have sufficient low-to-high frequency response is simpler than converting three-phase system components into equivalent single-line CM and DM models [21]–[24]. The proposed three-phase model is suitable for both time-domain and wide-spectrum frequency-domain analyses in DM and CM circuits to fully understand EMI problems.

To study motor-bearing current issues, single-line independent CM models have been extensively used in the literature to analyze shaft voltage and bearing current [25]–[32]. It is shown that existing bearing current models are only slightly modified for retrofit in the proposed three-phase universal motor model.

In this paper, a three-phase model for induction motors is presented to study the motor terminal overvoltage phenomena. The model is universal due to the fact that CM, DM, and bearing models are all combined into one circuit.

In Section II, the impedance variation versus frequency up to 10 MHz is examined using two three-phase induction motors, namely 5 and 20 hp, with a random wound stator winding in the Y- and Δ -connections, respectively. In Section III, the low- and high-frequency modeling of induction motors are generally discussed as an introduction to the proposed model. In Section IV, the proposed three-phase model for a wide frequency range is introduced, and the DM and CM frequency responses are examined using the experimentally obtained data of three 460-V four-pole induction motors, namely 5, 20, and 100 hp (Tables I and II). In Section V, the experimental and simulation results obtained from running the 100-hp motor by

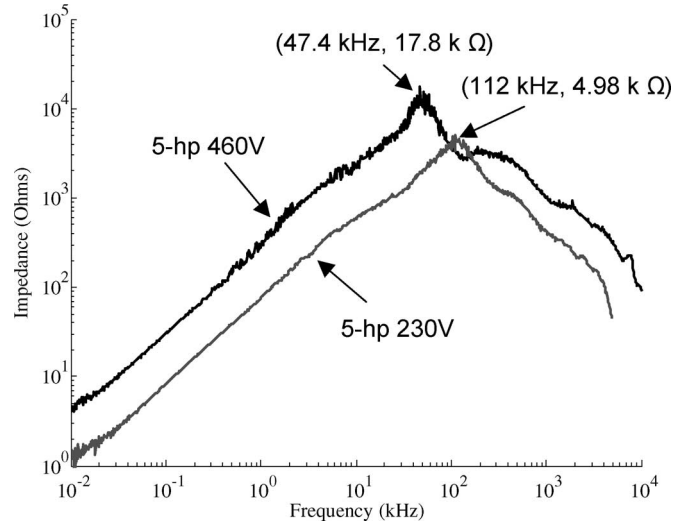


Fig. 1. Measured 5-hp induction motor DM impedance (magnitude) values versus frequency for two different winding connections, namely, 230 and 460 V.

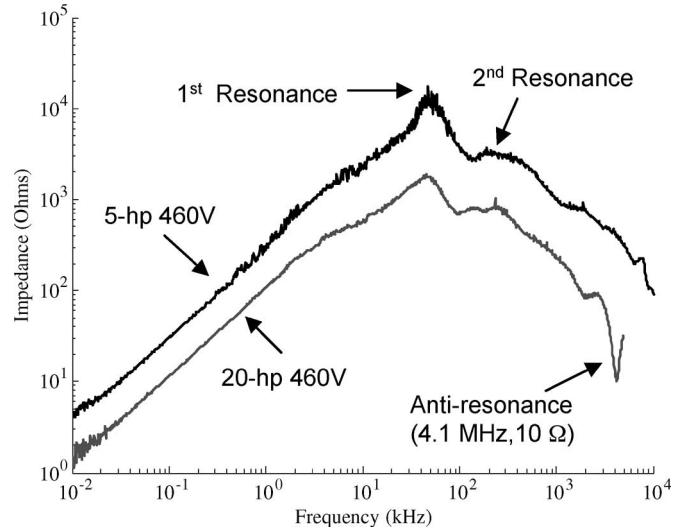


Fig. 2. Measured 5- and 20-hp induction motor DM impedance (magnitude) values versus frequency for a 460-V winding connection.

a voltage source PWM inverter through 40 m of shielded cable are presented to validate the proposed model.

II. INDUCTION MOTOR TRANSFER FUNCTION

In this section, the induction motor impedance versus frequency characteristics are examined, and the effects of motor geometry and winding connection on the impedance response are analyzed.

A. DM Transfer Function of Induction Motor

Fig. 1 shows the experimentally obtained DM impedance versus frequency of a 5-hp induction motor investigated for 460- and 230-V stator winding connections, which respectively correspond to internal series and parallel connections. Also, Fig. 2 shows the experimentally obtained DM impedance

versus frequency of both 5- and 20-hp motors for a 460-V stator winding connection only.

Fig. 1 demonstrates that the motor stray capacitors are mainly a function of motor geometry. Low-frequency motor impedance values below the first resonance are mainly L - R equivalent circuits. In this region, the impedance of the series 460-V connection has four times the value of the parallel 230-V connection since a winding inductance varies as N^2 (see Fig. 1 at 100 Hz). Fig. 1 also shows that the first resonance frequency of the 5-hp series connection is almost half the resonance frequency (f_r) of the parallel motor connections.

The f_r of the motor impedance is defined as where the impedance has its maximum magnitude and is calculated by $f_r = 1/(2\pi\sqrt{LC})$, where L and C are the effective inductance and capacitance values, respectively. The effective inductance L for a series connection is four times the value in a parallel connection, and f_r is half that of the parallel connection. Accordingly, the conclusion is that the motor stray capacitance does not significantly vary with changes in stator winding configuration. That is, in this case, the effective capacitance value C is mainly a function of the motor geometry or the motor frame size. It will be shown in Section IV that Y- and Δ -connections have impacts on the equivalent capacitance value at high frequencies.

The second objective of this section is to introduce the low-impedance antiresonance phenomenon observed in the case of the 20-hp motor at 4.1 MHz in Fig. 2. The motor impedance at this resonance frequency is $10\ \Omega$. This DM low impedance at 4.1 MHz will be approximately equivalent to $2.2\ \Omega$ in the CM circuit. This provides a very low impedance path for the CM leakage current at the low-impedance antiresonance. Thus, modeling of this phenomenon is of significance for EMI analysis in long cable motor drive systems. It is shown later that the so-called antiresonance is actually caused by the inductance of the first few turns of the winding. These observations are further discussed in Section IV, where the proposed motor model is derived based on the IEEE Standard 112 (T-equivalent) circuit.

B. Testing of DM Transfer Function

DM testing was performed with the phase-A motor lead as one probe and the phase-B and phase-C motor leads tied together to form the second probe. The measurements were taken using HP4284 (20 Hz to 1.0 MHz), HP4285 (75 kHz to 30 MHz), and AP200 (20 Hz to 15 MHz) *LCR* meters in Z - θ (impedance magnitude and phase angle) mode [33], [34]. The recommended test procedure is to use an ungrounded motor frame. It was observed that grounding the motor frame resulted in significant measurement errors at high frequency. This is attributed to errors in the instrument's impedance calculation procedure due to the *LCR* meter's two-lead source voltage driving capacitive current to ground that does not return on the two leads [35].

C. Testing of CM Transfer Function

CM testing was performed with the motor frame as one probe and the phase-A, -B, and -C motor leads tied together to form

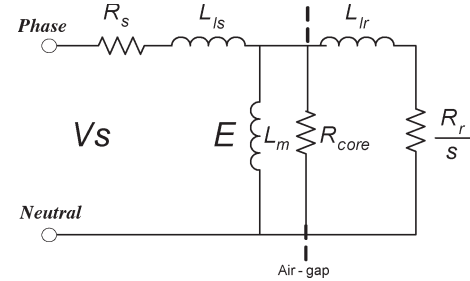


Fig. 3. IEEE 112 recommended per-phase low-frequency equivalent circuit.

the second probe. Impedance measurements versus calculated DM and CM transfer functions using the proposed induction motor model are demonstrated later in Section IV-E.

III. MODELING INDUCTION MOTOR FREQUENCY RESPONSE

In this section, existing lumped- and distributed-parameter models for the analysis of the low- and high-frequency behavior of induction motors are described.

A. Low-Frequency Response of Induction Motor

The low-frequency response of the polyphase induction motor has historically been studied since its origin. The IEEE Standard 112 was established to obtain test methods and parameters for a low frequency (50, 60, and 400 Hz) per phase T-equivalent induction motor model in Fig. 3 [36]. The rotor circuit and neutral are actually physically isolated from the line side stator neutral by the air gap in Fig. 3. Also, the rotor frequency (slip frequency) is different from the stator (or line) frequency. Users desire this low-frequency transfer function model to obtain the line side electrical quantities (frequency, current, power factor, and efficiency) for the given mechanical output quantities (power, horsepower, and torque). For convenience of analysis, rotor electrical quantities have thus been referred by stator-to-rotor turns ratio to the stator with an *implied* electrical connection to the stator neutral. In the low-frequency range, the applied voltage is uniformly distributed through the stator winding coils. Substantial literature exists on obtaining these model parameters from mathematical calculations, heuristic equations, and finite-element analysis (FEA). IEEE Standard 112 is a universally accepted test method to verify the accuracy of these model parameters that are readily obtainable by all users.

B. Mid-Frequency Response of Induction Motor

An accurate mid-frequency response (400 Hz to 20 kHz), as related to PWM ac drives, would be correlated with the carrier frequency motor ripple current and its associated heating in the motor copper and core laminations.

C. High-Frequency Response of Induction Motor

The high-frequency response of the polyphase induction motor has recently been studied. High-frequency motor

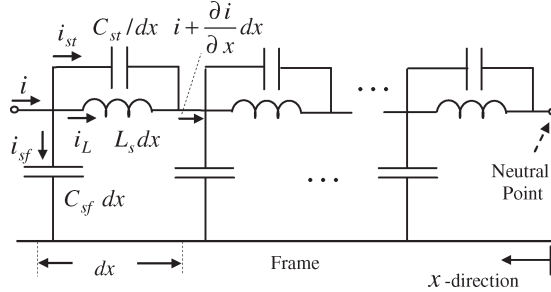


Fig. 4. Distributed high-frequency parameter model for stator windings.

models can be mainly divided into two classes, i.e., distributed and lumped parameter models. The initial need concerned the analysis of high-frequency high-magnitude surge effects on the utility-connected motor stator windings [4], [8]. Analysis methods typically include use of a distributed parameter model in Fig. 4 to analyze the distribution of surge voltage within the winding. FEA methods have been used to obtain a distributed parameter model for the analysis of the over-voltage and voltage ringing phenomena at the terminals of induction motors, which are associated with the interaction of motor surge impedance, long cable surge impedance, and PWM drive operation [36]. This paper showed that the rotor circuit is not involved in any high-frequency-related effects due to the minimal flux penetration into the rotor circuit at high frequencies. Investigations of [5] further show that the high-frequency-voltage rise-time-related effects of ASDs on the DM-reflected wave voltage at the motor terminals is mainly confined to the first few turns and at most the first coil group in a multicoil motor winding. This suggests that the low-frequency rotor circuit parameters need not be modified since it has no effect at high frequencies. Then, to obtain a high-frequency model, the first of many distributed sections of Fig. 4 is integrated into the existing low-frequency portion of Fig. 3.

High-frequency motor models have a response that is predominantly capacitive. These circuits are needed for the analysis of CM leakage current that occurs due to the interaction of line-to-ground stator winding slot capacitance with PWM drives. This is the main cause of EMI in ASD systems [20]. Also, the bearing current and shaft voltage models are capacitive in nature [25]–[32]. The existing problem in the field today is that researchers are proposing various individual high-frequency circuits [9], [15], [16], [21]–[24] to describe the reflected wave, CM current, and bearing current/shaft voltage. Indeed, many of them only address one issue and in addition ignore the low-frequency desired electrical stator quantities and rotor mechanical output quantities. Most of these high-frequency circuit models typically have parameters with no direct correlation to the induction motor geometry, since they are curve fitted to match a desired transfer function.

Thus, this paper proposes a three-phase universal induction motor model that is an extension of the standard T-equivalent circuit. This model unifies CM, DM, and bearing circuit models over the 10-Hz–10-MHz frequency range and has extended parameters that are realizable based on machine

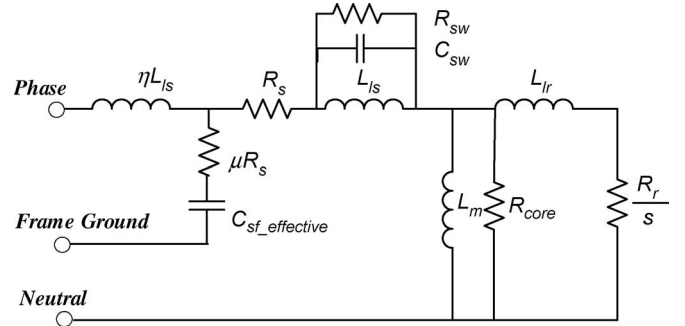


Fig. 5. Proposed per-phase universal induction motor model.

geometry. The proposed motor model is introduced in the next section.

IV. PROPOSED MODEL

To construct an accurate low-to-high frequency range transfer function model of the induction motor, one significant objective of this paper was to build the needed mid-to-high frequency circuit model extension around the existing and accurate physical realizable quantities of the standard low-frequency equivalent circuit.

A. Proposed per-Phase Universal Induction Motor Model

Motor behavior at steady-state conditions and low frequencies is best described by the well-known standard T-equivalent circuit in Fig. 3. In the low-frequency range, the voltage is distributed uniformly through the stator winding turns. In the medium-frequency range, the motor behavior can be best represented by a distributed parameter model in which the impact of rotor circuit is negligible and the motor behavior alternates between being capacitive and inductive. However, in this paper, motor behavior from 10 Hz to 10 MHz is studied. In this frequency range, typically one antiresonance and two resonances are observed, as detailed in Section II.

In order to model the aforementioned resonance and antiresonance frequencies, three capacitors $C_{sf\text{-effective}}$, $C_{sf\text{-}0}$, and C_{sw} are proposed as additions to the T-equivalent motor model in Fig. 3 to represent the mid-to-high frequency range of motor behavior characteristics. C_{sf} capacitance is the total stator-to-frame capacitance. $C_{sf\text{-effective}}$ is the effective stator-to-frame capacitance of the first slot per phase in Fig. 5. $C_{sf\text{-}0}$ is the stator-to-frame capacitance in the Y neutral. C_{sw} capacitance is the stator interturn capacitance per phase. Fig. 5 shows the proposed motor model in which the resonance frequencies are obtained by shorting all resistors and solving the quadratic equation $\alpha(\omega_r^2)^2 - \beta\omega_r^2 + 1 = 0$. Thus, we have

$$f_{r1} \text{ and } f_{r2} = \frac{1}{2\pi} \sqrt{(\beta \pm \sqrt{\beta^2 - 4\alpha})/2\alpha} \quad (1)$$

where $\alpha = L_{ls}L_{lr}C_{sw}C_{sf}$, $\beta = (L_{ls} + L_{lr})C_{sf} + L_{ls}C_{sw}$, and $f_{r1} < f_{r2}$.

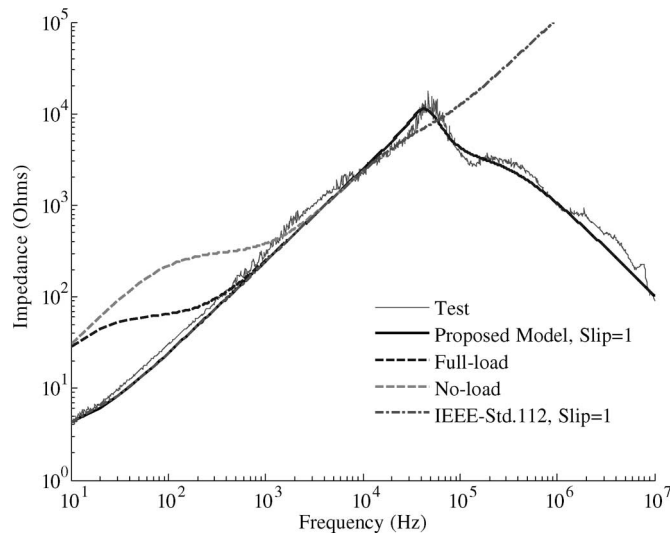


Fig. 6. Measured (Slip = 1) versus calculated 5-hp 460-V induction motor DM impedances (magnitude) versus frequency.

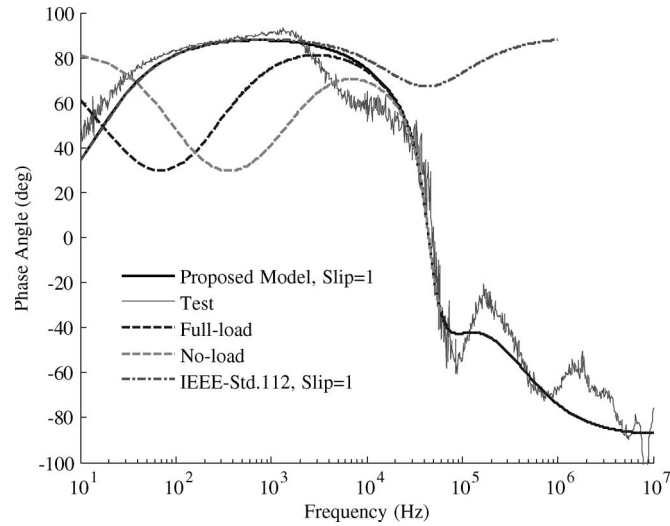


Fig. 7. Measured (Slip = 1) versus calculated 5-hp 460-V induction motor DM impedances (phase angle) versus frequency.

It should be noted that in (1), the effect of the magnetizing inductance is negligible since L_m is in parallel with the rotor leakage inductance L_{lr} and the fact that $L_m \gg L_{lr}$.

As a result of including C_{sf} -effective and C_{sw} capacitors into the standard T-equivalent circuit, this circuit represents the motor behavior over a wide range of frequencies, as shown in Figs. 6 and 7. In order to verify the proposed motor model, two induction motors were randomly selected and tested using a frequency analyzer. Measured results under LCR test have $s = 1$, and the frequency responses obtained from the proposed model calculations are compared in Figs. 6 and 7. In these figures, the motor's impedance frequency response, magnitude, and phase angle are shown over a wide range of frequencies from 100 Hz to 10 MHz. These figures also show the calculated impedance frequency response for rotor full load slip $s = 0.027$. As observed, motor speed (or motor load level) has no significant impact on motor impedance over the mid-to-high

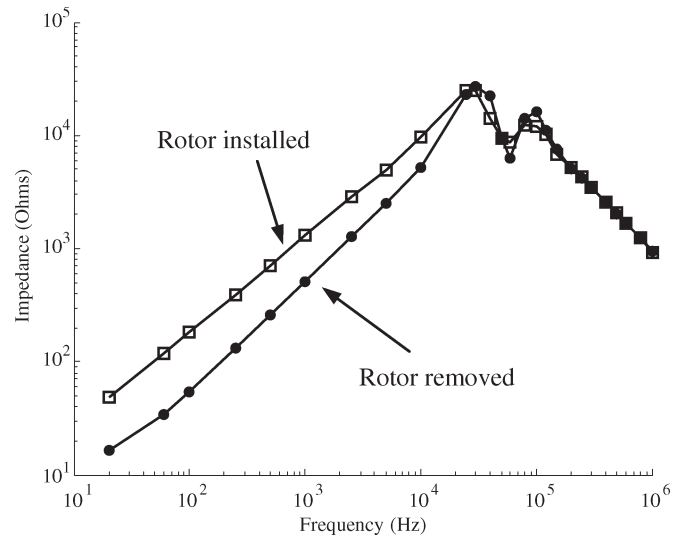


Fig. 8. Measured 1-hp 460-V induction motor impedance (magnitude) versus frequency: the influence of removing the rotor on the DM impedance transfer function [14].

frequency range. The proposed model curves closely match the high-frequency DM curve as well as the first and second resonance points. The T-Equivalent circuit shows correct motor impedance only up to f_r , as expected, due to the lack of resonance capacitors. This observation is explored further in Section VI.

A key issue is being able to match both DM and CM transfer functions for all frequencies in the proposed model knowing skin and proximity effects versus frequency exist. In the following subsection, the effect of rotor circuit will be discussed followed by a parameter identification procedure that insures both DM and CM transfer functions are correct.

B. Rotor Influence at High Frequency in the Proposed Model

Fig. 8 shows that the basic $L-R$ series impedance below resonance is lowered due to the removal of L_{lr} and $R_{r/s}$. Reflected wave overvoltage and EMI analysis is concerned with frequencies correlated with voltage pulse rise time defined by $1/(\pi t_r)$. Typical ASD rise times of 20 ns–2 μ s result in a frequency range of 150 kHz to 16 MHz. Fig. 8 demonstrates that the DM impedance is strictly dictated by stator parameters, so the low-frequency rotor circuit can be left as is in the new proposed model without error as could also be concluded from Figs. 6 and 7 under full-load and no-load conditions.

C. Parameter Identification Procedure for Proposed Model

1) *Stator Resistance R_s* : To insure that the fundamental frequency (50, 60, or 400 Hz) current flow in the model results in correct output fundamental power and torque, the R_s value must be the manufacturer's hot or cold resistance of the winding. Wire copper losses at harmonic frequencies, carrier frequency, and reflected wave ring frequencies must be accounted for in the R_{sw} damping term.

2) *Core Loss Resistance R_{core}* : R_{core} and L_m appear to have an effect on rounding the reflected wave ringing wave

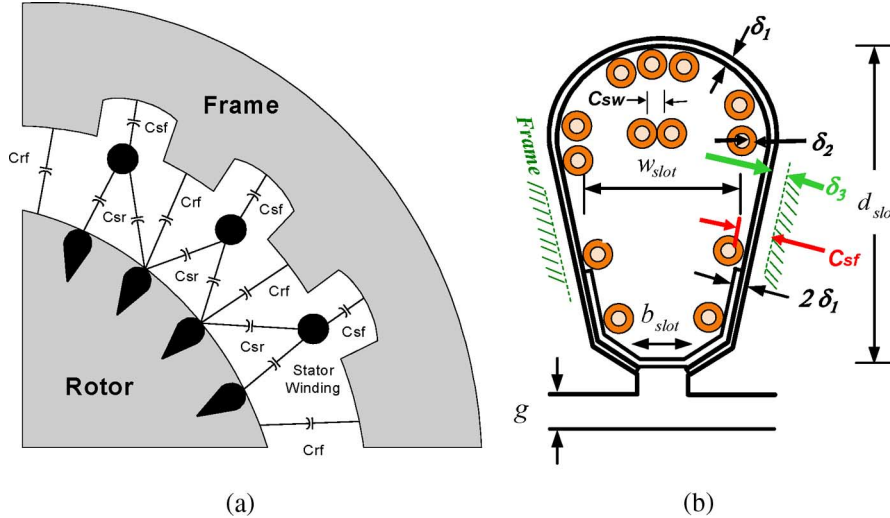


Fig. 9. Stator winding capacitances. (a) C_{sf} capacitance-to-ground. (b) Stator C_{sf} -slot slot capacitance-to-ground.

shape. For one specific manufacturer, the standard 460-V 60-Hz four-pole motor R_{core} values versus horsepower size were found to follow $R_{core} = 6300 \text{ (hp)}^{-0.6958}$. The importance of R_{core} is greater at higher horsepower, where it affects the terminal reflection coefficient by approaching the 50- to 120- Ω cable surge impedance values defined in [3].

3) *Rotor Resistance R_r , Rotor Inductance L_{lr} , and Slip s* : Section IV-B justifies using the manufacturer T-equivalent circuit values as is for the proposed motor model. There is rotor inductance skin effect and deep bar skin effects of rotor resistance, but these variations do not appreciably change the shape of the DM impedance curve versus frequency.

4) *Magnetizing Inductance L_m* : The IEEE Standard 112 fundamental frequency circuit value is used. It should be noted that the effect of the magnetizing inductance is negligible since it is in parallel with the rotor leakage inductance in helping define (1) resonance frequencies.

5) *Stator Leakage Inductance L_{ls}* : The IEEE Standard 112 fundamental frequency circuit value is also used. However, the reduction of L_{ls} inductance at harmonic and carrier frequencies is recognized to be a secondary effect. This may account for not having perfect matching of the DM transfer function over the entire frequency range.

6) *Stator First Turn Leakage Inductance ηL_{ls}* : This term is one of the critical parameters in defining the DM motor high-frequency impedance, predicting the antiresonance point of Fig. 2, and setting correct EMI leakage current to ground in the CM circuit. The term ηL_{ls} is used to account for the fact that only a fraction of the total stator leakage inductance is attributed to the high-frequency antiresonance point (~ 3 –10 MHz), specifically the first few turns in the first slot of the entry winding. Thus, ηL_{ls} is $(\text{the first few turns in the first slot/total turns per phase})^2 \times L_{ls}$. Winding data and machine geometry could be obtained from the manufacturer. The antiresonance point and ηL_{ls} are further discussed in Section IV-D.

If the value of ηL_{ls} is too high, then this inductance isolates the rest of the winding from the cable, and what appears in the reflected wave DM simulation is a wave shape that takes on the

appearance of an ideal open circuit. If ηL_{ls} is high, then this inductance also isolates the C_{sf} -slot term, and the current-to-ground peak and ring wave shape will not be correct in the CM simulation.

7) *Total Stator-to-Frame Capacitance per Phase $C_{sf-total}$* : Fig. 9(a) shows a physical representation of C_{sf} stator winding capacitance to frame ground. For frequencies greater than the first resonant frequency (f_{r1}), the stator slot winding-to-frame capacitance ($C_{sf-slot}$) plays an important role in describing the DM and CM motor behavior at high frequencies, while $C_{sf-total}$ plays a role in matching the CM transfer function at low frequency. $C_{sf-total}$ is calculated from the machine geometry by analyzing each slot capacitance to ground and multiplying by the number of stator slots. Each stator slot can be approximately considered as a rectangular-shaped conductor with L_{stack} stator length, w_{slot} average width, and d_{slot} average depth [see Fig. 9(b)]. Assuming all sides of this conductor are equipotential, the capacitance value between the conductor (stator windings in each slot) and the motor frame can be obtained as

$$C_{sf-slot} = \frac{\epsilon_0 L_{slot} L_{stack}}{\frac{k_t \delta_1}{\epsilon_{r1}} + \frac{\delta_2}{\epsilon_{r2}} + \frac{\delta_3}{\epsilon_{r3}}} \quad (2)$$

where L_{slot} is the stator slot circumference that can be approximated as $L_{slot} \approx 2d_{slot} + 1.5w_{slot}$, and δ_1 ($0.38 < \delta_1 < 0.63$ mm) and δ_2 ($0.38 < \delta_2 < 0.63$ mm) are the thicknesses of the slot wall and wire insulations [see Fig. 9(b)] with relative permittivity of ϵ_{r1} ($3.0 < \epsilon_{r1} < 3.2$) and ϵ_{r2} ($3.5 < \epsilon_{r2} < 4.0$), respectively. The slot wall insulation is 0.35–0.6 mm (~ 0.014 – 0.024 in) Class F Duroid polyester fiber paper with heat-resistant resin. As seen in Fig. 9(b), the top stick insulation is double along some part of the stator wall. Accordingly, a correction thickness factor of $1.0 < k_t < 1.5$ is defined here to take into account this extra insulation thickness. A third important factor in Fig. 9(b) is the possibility of a random small air gap ($0.02 < \delta_3 < 0.3$ mm) between the slot liner-to-frame. The effective $C_{sf-total}$ and $C_{sf-slot}$ may change by 2:1 with

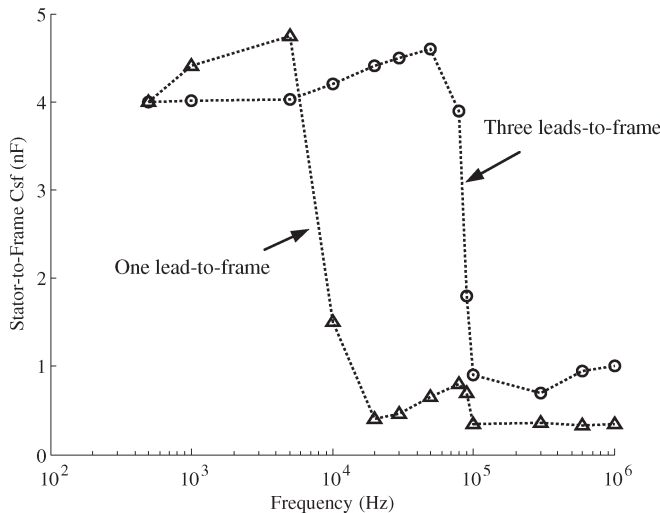


Fig. 10. Measured stator winding capacitances-to-frame for the 5-hp motor.

TABLE III
5-, 20-, AND 100-hp INDUCTION MOTORS'
CALCULATED CAPACITANCE VALUES

Capacitance Values	5 hp	20 hp	100 hp
$C_{sf\text{-slot}}$ (nF)	0.213	0.409	0.703
$C_{sf\text{-effective}}$ (nF)	0.213	0.818	2.80
$C_{sf\text{-total}}$ (nF)	3.834	9.815	21.05
$C_{sf\text{-0}}$ (nF)	3.195	7.361	12.65
C_{sw} (nF)	0.852	1.63	5.60

liner air gaps, which makes calculations less precise. For a motor with N_{slot} stator slots and a *double-layer* winding, the total stator winding to frame capacitance can be obtained as

$$C_{sf\text{-total}} = (N_{\text{slot}} \times C_{sf\text{-slot}})/2. \quad (3)$$

8) *Stator-to-Frame Capacitance $C_{sf\text{-slot}}$ and $C_{sf\text{-effective}}$:* Fig. 10 shows the measured frequency variation of C_{sf} for one motor lead and C_{sf} for all three leads tied together with respect to frame ground. Note that the one-lead capacitance is much lower in the 100-kHz to 16-MHz range than the low-frequency value, and that it is also constant. This is explained using the distributed parameter model in Fig. 4. At low frequencies, the entire summation of multiple sections contributes to C_{sf} , but at high frequencies, only one section is functional, and the rest are impedance isolated. The 300-pF value for frequencies greater than 100 kHz agrees with the calculated $C_{sf\text{-effective}}$ for one slot in Table III and verifies the single-slot theory for DM high-frequency response. Note that the three-lead CM measurement in Fig. 10 for frequencies greater than 100 kHz is approximately three times the single-lead value. This is because the first distributed sections of all three leads are the only sections contributing in parallel, so the three-lead value is approximately three times the one-lead value. Note also that the one-lead and three-lead measurements at low frequency are not three times but the same value. This is because the single-lead value can go through the motor neutral and pick up the stator-to-frame capacitance in the other two phases. In the

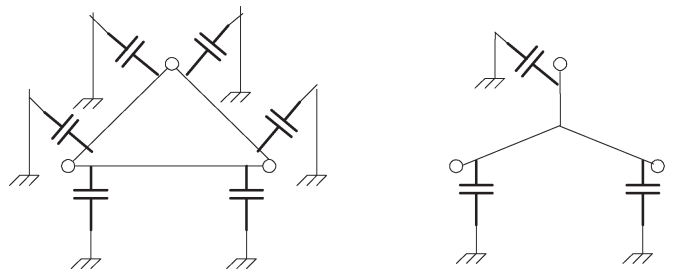


Fig. 11. Delta-wound machines have twice effective slot capacitances-to-ground.

10- to 100-kHz range, the three-lead value is picking up more end-terminal-distributed sections so its value is higher than the one-lead measurement.

Another machine geometry factor in Fig. 11 is that a Δ -connection has twice $C_{sf\text{-slot}}$ compared to a Y-connection. Moreover, the number of parallel circuits may also change the effective stator-to-frame capacitance value $C_{sf\text{-effective}}$.

9) *CM Stator-to-Frame Capacitance $C_{sf\text{-0}}$:* Based on prior discussion, $C_{sf\text{-0}}$ is the remaining stator CM capacitance-to-ground lumped in the neutral Y. Accordingly, the following value is used in the proposed three-phase model:

$$C_{sf\text{-0}} = C_{sf\text{-total}} - 3C_{sf\text{-effective}}. \quad (4)$$

10) *Stator Turn-to-Turn Winding Capacitance C_{sw} :* This parameter can be determined in a number of ways. The first heuristic method is based on many tests performed in a previous work on more than 50 different motors [14], and noting that the second resonance frequency is approximately twice or less than the first resonance frequency. That is, the interturn stray capacitance can be obtained as a function of $C_{sf\text{-effective}}$, $C_{sw} = (f_{r2}/f_{r1})^2 C_{sf\text{-effective}}$. The second method is to solve (1) for C_{sw} assuming f_{r1} is known.

11) *Stator Turn-to-Turn Damping Resistance in Winding R_{sw} :* This term accounts for the skin and proximity effect of the wire and high-frequency core loss. Quite simply, at first resonance peak (Fig. 2), the DM impedance measured is equal to $(3/2)R_{sw}$, i.e., the damping resistance for a parallel resonant circuit. It has been found that the core loss resistor R_{core} does not have a significant impact on damping. Calculation of wire skin and proximity effects for the wire thickness used is possible but beyond the scope of this paper. The wire skin and proximity effect factors at the resonant frequency multiplied by the R_{dc} value results in a series value that could be converted to a parallel R_{sw} value.

12) *Stator Initial Frame-to-Ground Damping Resistance μR_s :* This component is the ac resistance of the fractional part of the total stator R_s due to the ηL_{ls} segmentation described. The 60-Hz μR_s value is proportional to the stator resistance, and a multiplying factor of 10–20 is used for ac skin and proximity effects. In addition, it also encompasses the resistivity of steel laminations from the slots to where the motor ground wire in the junction box is connected. This value needs further research and was not accounted for in this paper. The term

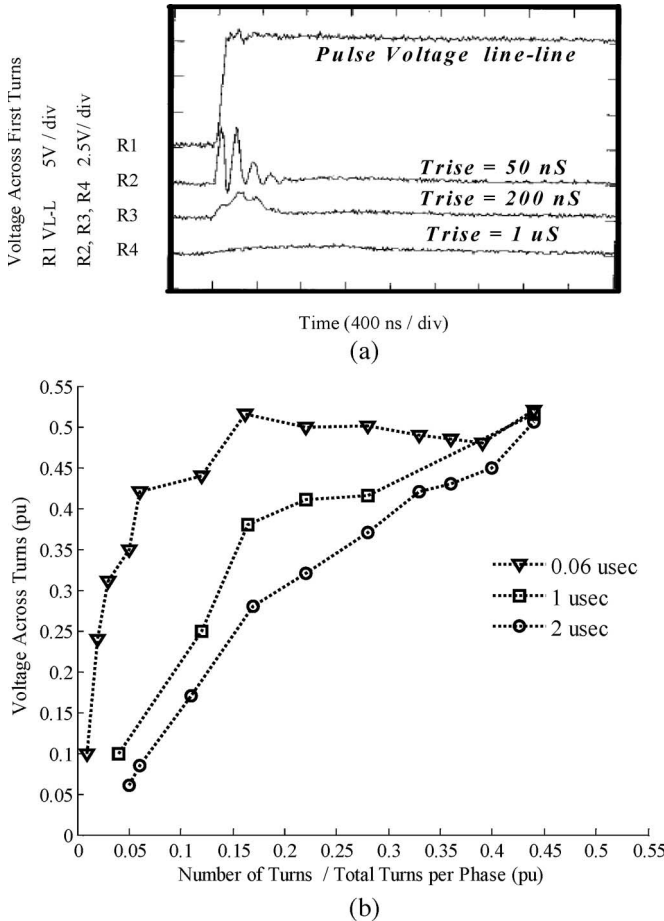


Fig. 12. Tapped stator winding from [5] used to justify the antiresonance point. (a) Measured stator winding voltage from end turn to first few turns [5]. (b) Measured stator winding end voltage to tap in per unit versus tap turn #/total turns.

μR_s affects the peak CM current as well as the damping of oscillations in the CM current to ground.

D. Antiresonance Phenomenon

This section investigates the correlation between tapped stator testing with the 4.5-MHz antiresonance phenomenon observed in Fig. 2. A six-pole 7.5-hp 460-V tapped stator motor in [5] was random wound with 19 turns per coil and 18 coils in series per phase for a total of 342 turns per phase. The 1- μs , 200-ns, and 50-ns pulse voltage rise times in Fig. 12(a) correspond to equivalent frequencies of 318 kHz, 1.6 MHz, and 6.3 MHz. The 1- μs and 0.2- μs rise times do not excite the antiresonant frequency, but the 50-ns rise time can excite the 5-MHz antiresonance point, which results in the oscillation of 200 ns (5 MHz, Fig. 12). DM antiresonance also occurred in the other motors tested.

Fig. 12(b) shows that the first few turns (four turns) divided by the total number of turns (342) result in “ $x = 0.02$ ” axis entry and a high 0.35-pu peak of line-to-line reflected wave voltage for 50-ns impulse-type voltage rise times. The first coil group at 0.16 pu has already obtained the highest peak voltage possible. These data justify that correct reflected wave

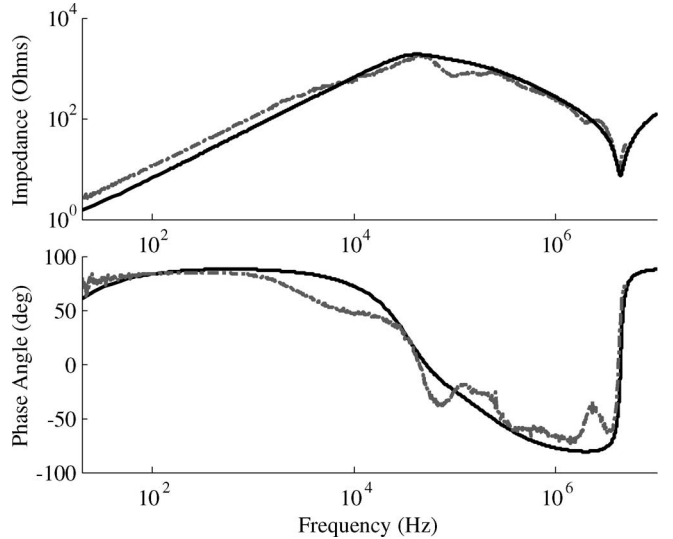


Fig. 13. Measured (dotted line) versus calculated (solid line) 20-hp 460-V induction motor DM impedance (magnitude and phase) values versus frequency.

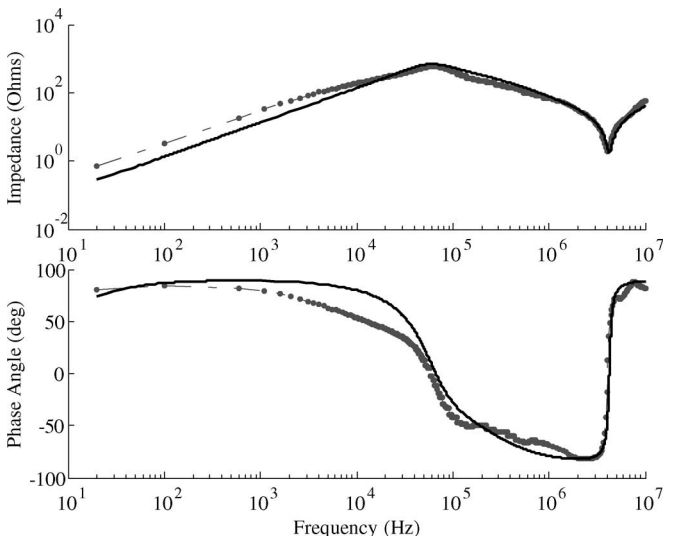


Fig. 14. Measured (dotted line) versus calculated (solid line) 100-hp 460-V induction motor DM impedance (magnitude and phase) values versus frequency.

waveforms are obtained by using just $C_{sf\text{-slot}}$ defined by the first coil and first slot.

E. DM/CM Transfer Function Verification of Proposed Model

To verify the proposed motor model, 20- and 100-hp induction motors were tested. The measured motor DM impedance frequency response using a frequency analyzer, which shows magnitudes and phase angles, are plotted over a wide 100-Hz to 10-MHz frequency range. Figs. 13 and 14 show good comparison between the test results and the proposed model calculated frequency response in both “*Magnitude and Phase Angle*.”

Of interest is the mismatch between the *LCR*-measured (then $s = 1$) DM impedance of the 100-hp Δ -connection and the proposed model impedance using the exact low-frequency

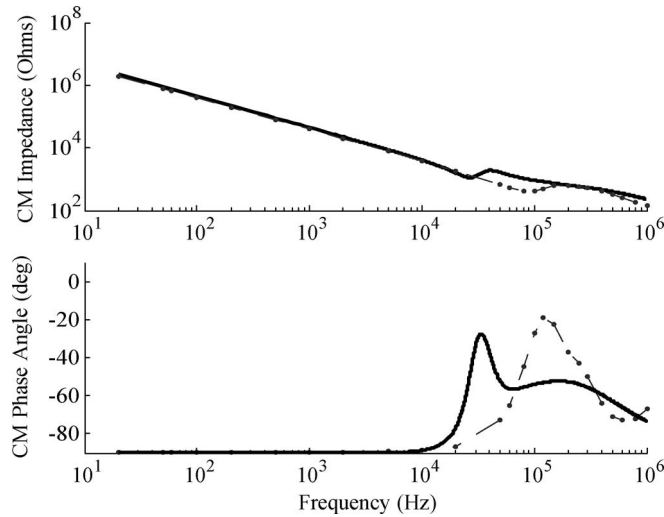


Fig. 15. Measured (dotted line) versus calculated (solid) 5-hp 460-V induction motor CM impedance (magnitude and phase) values versus frequency.

T-equivalent circuit components in the 20-Hz to 10-kHz range. The measured dc resistance with a milliohm meter was found to match the IEEE 112 R_s parameter. One explanation is that DM testing with two leads shorted to one LCR input and with another motor lead tied to the other LCR input energizes only two windings in a Δ -connection as opposed to a Y-connection where all three motor leads are energized. Also, the small exciting voltage (20 mV–2 V) from the LCR meter may bias the stator core in the very widely nonlinear part of the dc magnetization curve, which results in an incorrect L_m value. The DM impedance was indeed changing at frequencies less than 1 kHz as the LCR source voltage was varied. The proposed modified T-model with $s = 1$ assumes that the rotor leakage inductance L_{lr} is much less than L_m so that the input inductance is approximately equal to $L_{ls} + L_{lr}$. In reality, at low flux levels, the rotor N_s/N_r transformation may be isolated so that the input inductance appears mostly as the sum of L_{ls} and a widely varying L_m .

The measured versus proposed model that calculated the CM frequency response in Figs. 15 and 16 for 5 and 100 hp also shows a good match. The lumped C_{sf-0} in the neutral of Fig. 17 matches the low-frequency response, while $C_{sf-slot}$ matches the high-frequency response. The resonance impedance wave shape is similar but not exact in frequency value due to single lumped parameter selection.

F. Proposed Three-Phase Universal Induction Motor Model

Fig. 17 shows a three-phase version of the proposed universal induction motor model with the addition of the bearing current–shaft voltage model to the stator neutral.

G. Bearing Current/Shaft Voltage Model Addition

Fig. 18 shows prior CM equivalent system single-line models for shaft voltage/bearing current investigation [25]. Although small differences occur, this model has general agreement with other single-line-bearing models [26]–[31]. The inverter drive

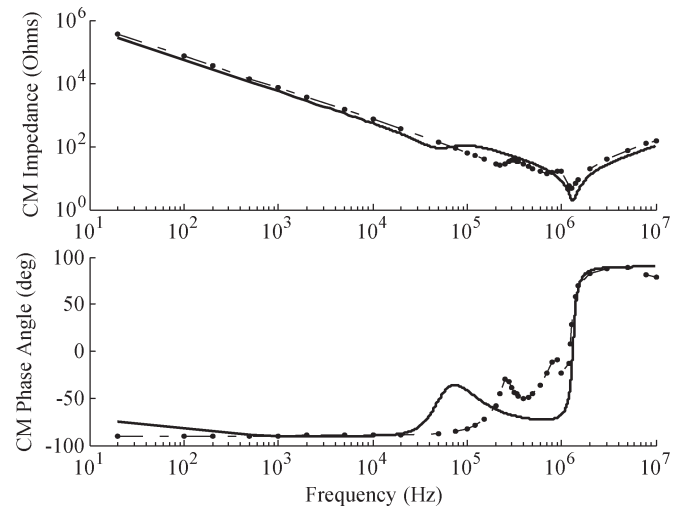


Fig. 16. Measured (dotted line) versus calculated (solid) 100-hp 460-V induction motor CM impedance (magnitude and phase) values versus frequency.

is shown as a stator neutral-to-ground zero-sequence voltage source (V_{sng}). The prior motor-bearing model in Fig. 18 consists of CM motor capacitances: CM stator-to-frame (C_{sf}), CM stator-to-rotor (C_{sr}) across the air gap, and CM rotor-to-frame (C_{rf}). Test procedures to obtain these motor zero-sequence parameters from the machine geometry as well as parameter variation with the motor's output power (in horsepower) were outlined in [36]. The bearing model combines the bearing ball/race resistance (R_b) in series with a parallel combination of the bearing oil film capacitance (C_b) and a nonlinear device (Z_l) accounting for the random charging and discharging of the rotor shaft due to asperity point contacts puncturing the oil film [38].

The proposed universal induction motor model for shaft voltage/bearing current investigation consists of a three-phase PWM inverter modulator, three-phase cable impedance, and modification to prior motor-bearing CM model circuit. The advantage of the new concept is that the three-phase modulated zero-sequence voltage generation V_{sng} vector directly interacts with the cable and motor circuits for any inverter operating point. The prior model V_{sng} waveform was offline estimated for a single operating point and recreated in the CM model.

The proposed motor-bearing circuit concept is as follows. Since V_{sng} is the stator neutral-to-ground zero-sequence voltage source, the prior CM-bearing model in Fig. 18 can be placed at the identical V_{sng} point in the proposed three-phase model (Fig. 17). The bearing voltage ratio (BVR) previously derived remains the same, since

$$\text{BVR} = \frac{V_{rg}}{V_{sng}} = \frac{C_{sr}}{C_{sr} + C_b + C_{rf}} \quad (5)$$

shows that BVR is the divider ratio only between motor CM capacitances C_b , C_{sr} , and C_{rf} from the V_{sng} source. The V_{rg} shaft voltage will remain as typically 10% to 15% of the stator neutral voltage switching pattern [38]. Modification from the prior bearing model is through removing the old CM C_{sf} from V_{sng} and splitting into first slot $C_{sf-slot}$ values in each phase

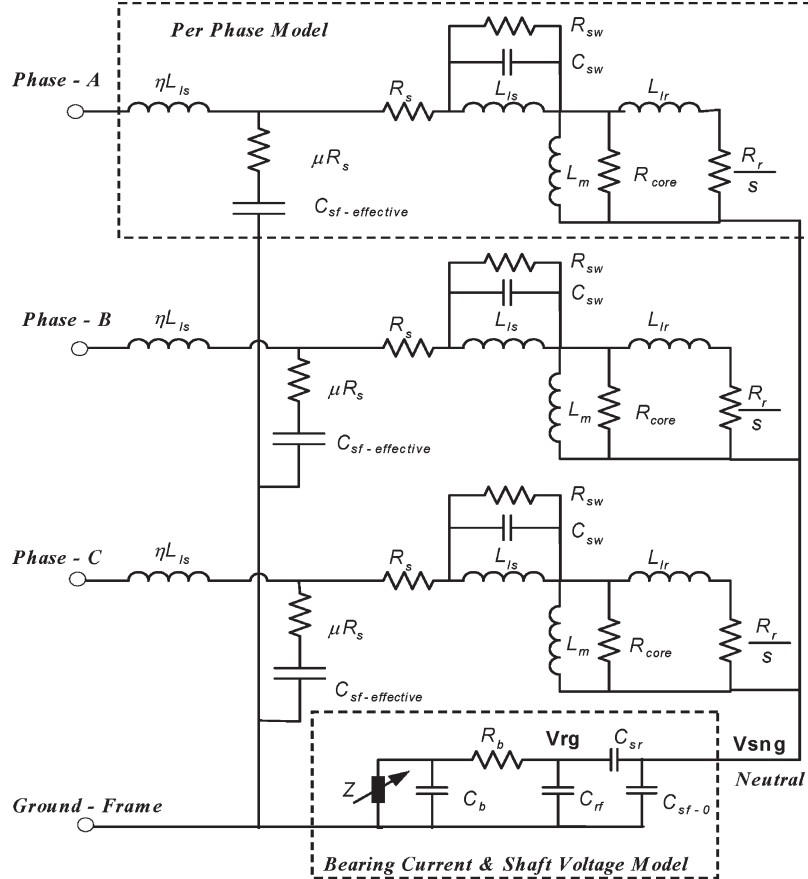


Fig. 17. Proposed three-phase universal induction motor model.

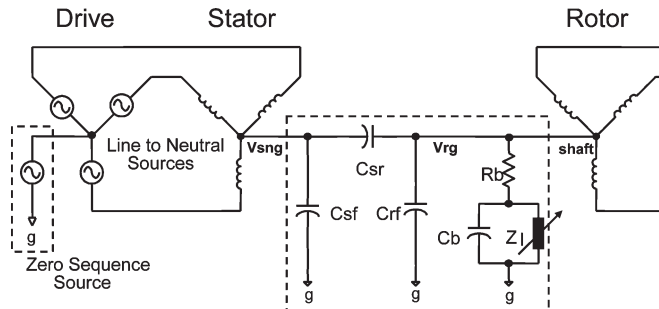


Fig. 18. Prior shaft voltage/bearing current single-line zero-sequence model [25].

in Fig. 5 and C_{sf-0} value lumped as a Y neutral component in Fig. 17. This performs the same bearing model function as well as providing accurate motor CM ground current waveforms and matching CM transfer function versus frequency.

V. VERIFICATION OF THE THREE-PHASE MODEL

A. Model Verification: Measured Versus Simulated Waveforms

A 100-hp motor was tested in Fig. 19 with a voltage-source PWM inverter with carrier frequency of 4 kHz through 40 m of #2 American wire gauge shielded cable. The system was also simulated with Matlab SimPowerSystems [17] using a distributed-parameter three-phase cable model that exists in the

toolbox and the proposed universal three-phase motor model in Fig. 17. The cable model in Matlab is based on Bergeron's traveling-wave method [8]. The cable parameter identification procedures for three-phase cables are found in [11]. The motor is assumed to operate at constant speed. Simulation results and corresponding test results are shown in Figs. 20–23.

Fig. 20(a) shows the simulated motor voltage. The reflected wave overvoltage due to the fast rise time IGBT is approximately 200% of the dc-bus voltage. Fig. 20(b) shows the experimentally obtained data. The simulation results are in very good agreement with the experimental data for peak values, waveform shape, and ringing frequencies. It is interesting how the added capacitors $C_{sf\text{-effective}}$ are involved with the line-to-line transient voltage.

Fig. 21(a) shows the CM current at the motor terminals from simulation, and Fig. 21(b) shows that with the experimental results. As seen, the CM current obtained from simulation is in good agreement with the experimental data. Accordingly, the proposed three-phase motor model can be used for both DM and CM system analyses. The ring frequency obtained from simulation closely matches the experimental data having $1.5\ \mu\text{s}$ (667 kHz) with some very high ring frequency (5 MHz) spikes that are excited. Damping times are $7\ \mu\text{s}$ in both simulated and measured waveforms. The peak simulation values are two times higher since a ferrite CM saturating inductor ($\sim 3\text{A } I_{\text{sat}}$) used in the drive was not simulated. Also, the motor steel lamination resistivity in the stack was not determined and modeled.

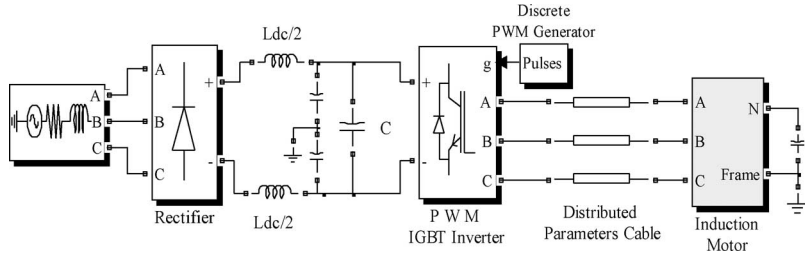
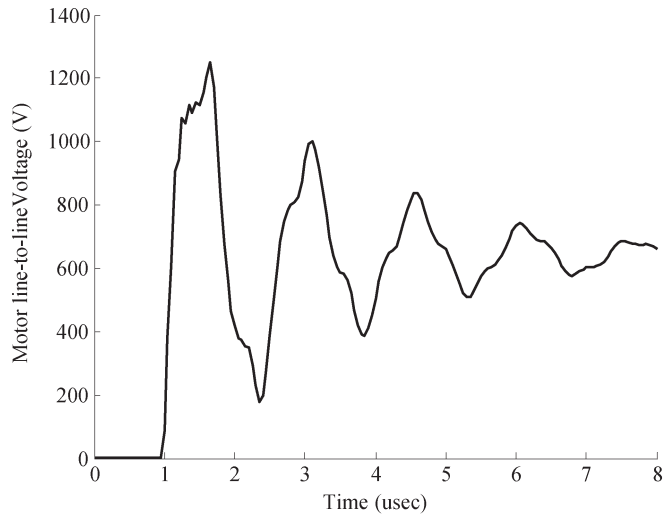
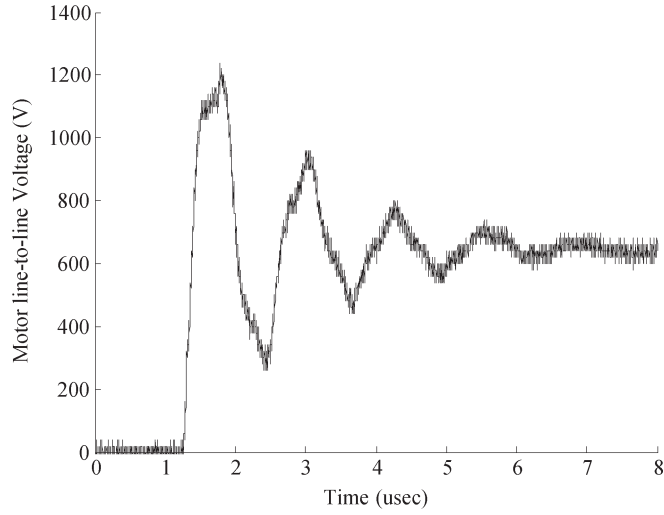


Fig. 19. Typical drive/long cable/motor system with distributed-parameter cable model of Matlab and proposed three-phase induction motor model.



(a)

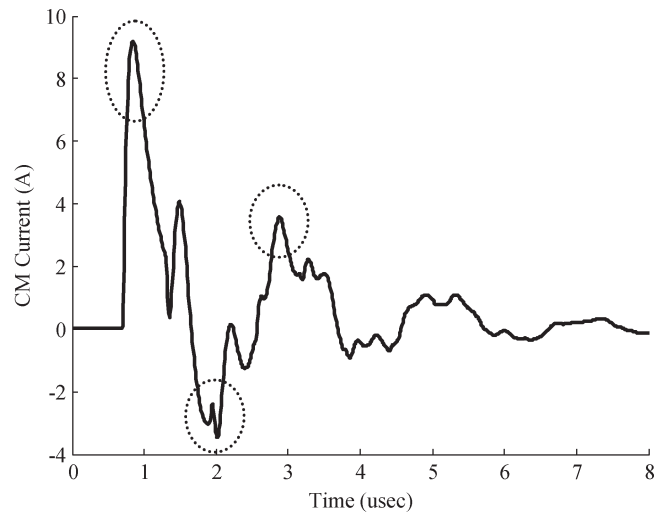


(b)

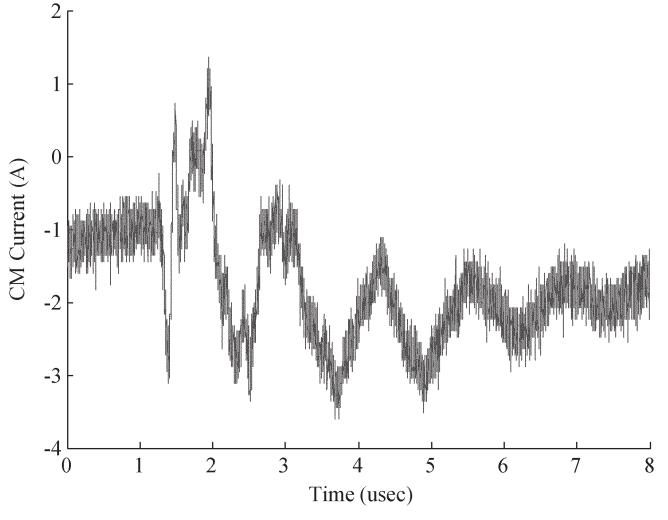
Fig. 20. (a) Motor voltage obtained from simulation results of the inverter (risetime = 200 ns)—cable (40 m)—induction motor (100 hp) system shown in Fig. 19. (b) Motor voltage obtained from experimental results of the inverter (risetime = 200 ns)—cable (40 m)—induction motor (100 hp) system shown in Fig. 19.

The stator neutral-to-ground voltage is simulated in Fig. 22(a) along with the shaft-to-ground voltage [Fig. 22(b)], which shows the BVR of 15% that is in agreement with that tested in prior work on bearing currents [25].

The line current is shown in Fig. 23(a) over one cycle. The significance being that not only is the fundamental low-frequency current for the operating point obtainable but also the



(a)



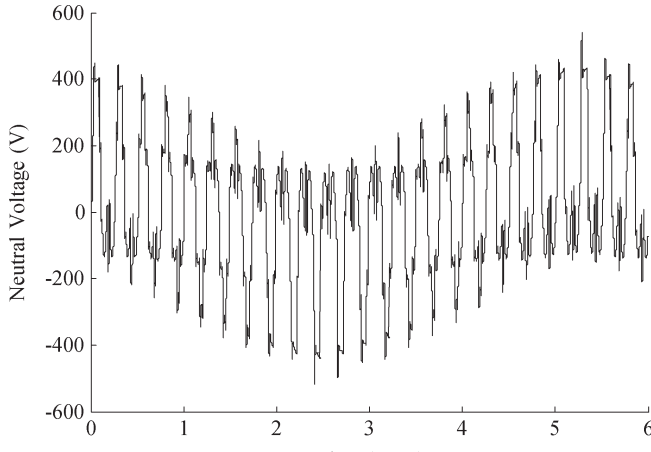
(b)

Fig. 21. (a) CM current simulated at 100-hp motor input terminals. (b) CM current measured at 100-hp motor input terminals.

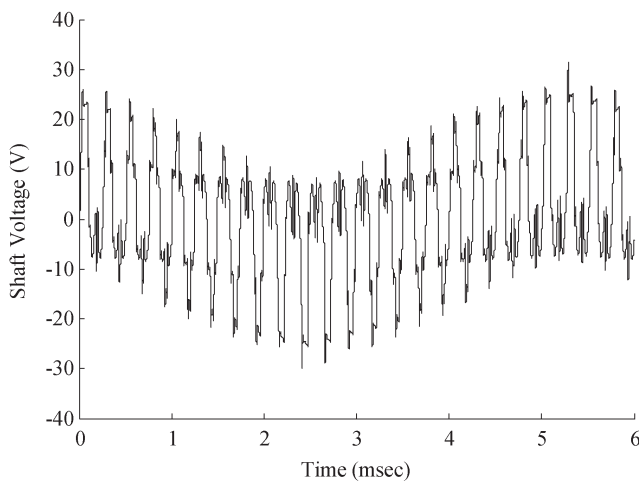
ASD carrier-based mid-frequency range ripple current and the high-frequency CM and DM motor line-charging current spikes are simultaneously visible in the expanded waveform shown in Fig. 23(b).

VI. OBSERVATIONS AND FUTURE WORK

This paper has developed a universal induction motor model based on a generic per phase model topology and using machine



(a)



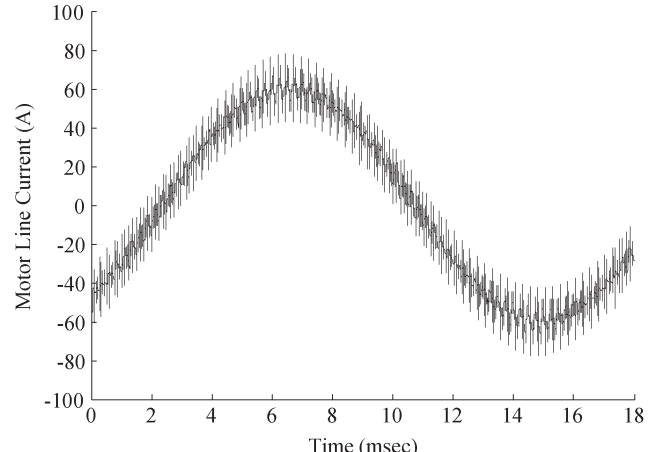
(b)

Fig. 22. (a) CM voltage at 100-hp motor input terminals. (b) Shaft voltage V_{rg} of 100-hp motor showing BVR divider action.

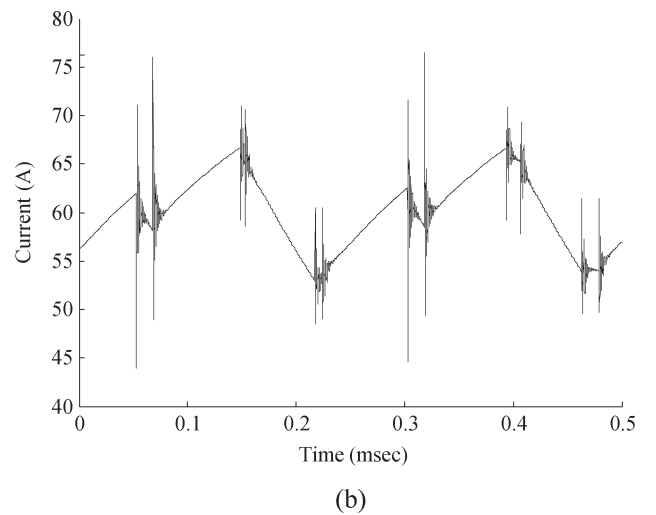
specifics to assist in determining the model parameters. An observation from magnitude and phase angle plots in Figs. 6 and 7 for the IEEE Standard 112 T-equivalent circuit with slip equal to 1 shows that the corresponding phase angle goes from 85° at low frequency, then dips to 70° at 47.4 kHz, and then rises back to 85° at higher frequency. The 47.4 kHz exactly corresponds to f_{r1} . Accordingly, the implication is that f_{r1} can be predicted even without knowing the stray capacitance values C_{sf} and C_{sw} from the impedance phase angle of the IEEE Standard 112 T-equivalent circuit while the slip is equal to 1. Future research needs to determine if this phenomenon is an anomaly or appears on every motor.

VII. CONCLUSION

In this paper, a new model for induction motors has been presented. The proposed model represents the motor's behavior over a wide range of frequencies and can be used for low frequencies as well as reflected wave, bearing current, and CM studies. Experimental results have been presented to validate the motor model for long cable applications on ASDs. The



(a)



(b)

Fig. 23. (a) Line current simulation of the 100-hp motor showing fundamental current, ripple current, and CM to ground current. (b) Expanded line current simulation of the 100-hp motor showing fundamental current, ripple current, and CM-to-ground current.

proposed model may also be used for the analysis of utility-generated surges on ac-line-connected motors.

ACKNOWLEDGMENT

The authors would like to thank M. Melfi and C. Jamison of Rockwell Automation/Reliance Electric for providing the induction motor parameters and D. Kirschner of Rockwell Automation/Allen-Bradley Mequon Drives for test support.

REFERENCES

- [1] R. Kerkman, G. Skibinski, and D. Schlegel, "Unintended consequence of low risetime IGBTs," presented at the International Electric Machines and Drives Conf. (IEMDC), Madison, WI, Jun. 2003.
- [2] E. Persson, "Transient effects in application of PWM inverters to induction motors," *IEEE Trans. Ind. Appl.*, vol. 28, no. 5, pp. 1095–1101, Sep./Oct. 1992.
- [3] G. Skibinski, "Design methodology of a cable terminator to reduce reflected voltage on AC motors," in *Conf. Rec. IEEE IAS Annu. Meeting*, San Diego, CA, Oct. 6–10, 1996, pp. 153–161.
- [4] A. Narang, B. K. Gupta, E. P. Dick, and D. K. Sharam, "Measurement and analysis of surge distribution in motor stator windings," *IEEE Trans. Energy Convers.*, vol. 4, no. 1, pp. 126–134, Mar. 1989.

- [5] M. Melfi, A. M. J. Sung, S. Bell, and G. L. Skibinski, "Effect of surge voltage risetime on the insulation of low-voltage machines fed by PWM converters," *IEEE Trans. Ind. Appl.*, vol. 34, no. 4, pp. 766–775, Jul./Aug. 1998.
- [6] G. Skibinski, J. Erdman, J. Pankau, and J. Campbell, "Assessing AC motor dielectric withstand capability to reflected wave stress using corona testers," in *Conf. Rec. IEEE IAS Annu. Meeting*, San Diego, CA, Oct. 6–10, 1996, pp. 694–702.
- [7] S. Bell and J. Sung, "Will your motor survive a new adjustable speed drive," in *Proc. IEEE PCIC*, Philadelphia, PA, Sep. 23–25, 1996, pp. 125–130.
- [8] H. W Dommel, "Digital computer solution of electromagnetic transients in single and multiple networks," *IEEE Trans. Power App. Syst.*, vol. PAS-88, no. 4, pp. 388–398, Apr. 1969.
- [9] G. Skibinski, R. J. Kerkman, D. Leggate, J. Pankau, and D. Schlegel, "Reflected wave modeling techniques for PWM AC motor drives," in *Proc. IEEE APEC*, 1998, pp. 1021–1029.
- [10] D. Hyypio, "Simulation of cable and winding response to steep fronted voltage waves," in *Conf. Rec. IEEE IAS Annu. Meeting*, Orlando, FL, Oct. 8–12, 1995, pp. 800–806.
- [11] G. Skibinski, R. Tallam, R. Reese, B. Buchholz, and R. Lukaszewski, "Common-mode and differential-mode analysis of 3 phase cables for PWM AC drives," in *Conf. Rec. IEEE IAS Annu. Meeting*, Tampa, FL, Oct. 6, 2006, pp. 880–888.
- [12] A. von Jouanne, P. Enjeti, and W. Gray, "The effect of long motor leads on PWM inverter fed AC motor drive systems," in *Proc. IEEE APEC*, Dallas, TX, Mar. 6–9, 1995, pp. 592–597.
- [13] D. Schlegel, G. Wrate, R. Kerkman, and G. Skibinski, "Resonant tank motor model for voltage reflection simulations with PWM drives," in *Proc. IEEE IEMDC*, Seattle, WA, May 9–12, 1999, pp. 463–465.
- [14] D. Schlegel, "Development of a high frequency induction motor model for reflected wave simulations," in *Masters Design Project*. Milwaukee, WI: Milwaukee School Of Engineering, Apr. 1999.
- [15] E. Zhong, T. A. Lipo, and S. Rossiter, "Transient modeling and analysis of motor terminal voltage on PWM inverter-fed AC motor drives," in *Conf. Rec. IEEE IAS Annu. Meeting*, Oct. 1998, pp. 773–780.
- [16] A. F. Moreira, T. A. Lipo, G. Venkataraman, and S. Bernet, "High-frequency modeling for cable and induction motor overvoltage studies in long cable drives," *IEEE Trans. Ind. Appl.*, vol. 38, no. 5, pp. 1297–1306, Sep./Oct. 2002.
- [17] *Matlab SimPowerSystems*. Natick, MA: The Math Works, Inc, 2006.
- [18] R. Kerkman, D. Leggate, and G. Skibinski, "Interaction of drive modulation and cable parameters on ac motor transients," in *Conf. Rec. IEEE IAS Annu. Meeting*, Oct. 1996, pp. 143–152.
- [19] A. M. de Broe, A. L. Julian, and T. A. Lipo, "Neutral-to-ground voltage minimization in a PWM-rectifier/inverter configuration," in *Proc. 6th Int. Conf. Power Electron. Variable Speed Drives*, Sep. 23–25, 1996, pp. 564–568.
- [20] G. Skibinski, R. J. Kerkman, and D. Schlegel, "EMI emissions of modern PWM AC drives," *Ind. Appl. Mag.*, vol. 5, no. 6, pp. 47–81.
- [21] A. Consoli, G. Oriti, A. Testa, and A. Julian, "Induction motor modeling for common mode and differential mode emission evaluation," in *Conf. Rec. IEEE IAS Annu. Meeting*, 1996, pp. 595–599.
- [22] M. Schinkel, S. Weber, S. Gutkowski, W. John, and H. Reichl, "Efficient HF modeling and model parameterization of induction machines for time and frequency domain simulations," in *Proc. IEEE APEC*, Dallas, TX, 2006, pp. 1181–1186.
- [23] A. Boglietti and E. Carpaneto, "Induction motor high frequency model," in *Conf. Rec. IEEE IAS Annu. Meeting*, Phoenix, AR, Oct. 1999, pp. 1551–1558.
- [24] A. Boglietti and E. Carpaneto, "An accurate induction motor high frequency model for electromagnetic compatibility analysis," *Electr. Power Components Syst.*, vol. 29, no. 3, pp. 191–205, Mar. 2001.
- [25] R. Kerkman, D. Schlegel, and G. Skibinski, "Characteristics of shaft voltage and bearing currents," *Ind. Appl. Mag.*, vol. 3, no. 6, pp. 21–32, Nov./Dec. 1997.
- [26] S. Chen, T. Lipo, and D. Fitzgerald, "Modeling of motor bearing currents in PWM inverter drives," *Trans. Ind. Appl.*, vol. 32, no. 6, pp. 1365–1370, Nov./Dec. 1996.
- [27] A. Muetze and A. Binder, "Calculation of motor capacitances for prediction of discharge bearing currents in machines of inverter based drive systems," in *Proc. IEEE IEMDC*, San Antonio, TX, May 2005, p. 264.
- [28] P. Link, "Minimizing electric bearing current in ASD systems," *IEEE Ind. Appl. Mag.*, vol. 5, no. 4, pp. 55–65, Jul./Aug. 1999.
- [29] K. Iimori, K. Shinohara, and M. Aikou, "A common mode equivalent circuit usable for calculating CM current and bearing current of induction motor driven by PWM inverter," *Trans. Inst. Electr. Eng. Jpn.*, vol. 125, no. 5, p. 438, 2005.
- [30] J. Ollila, T. Hammar, J. Lisakkala, and H. Tuusa, "A new reason for bearing current damages in variable speed drives," in *Proc. EPE*. Trondheim, Norway, Sep. 1997.
- [31] S. Gutkowski, S. Weber, M. Schinkel, W. John, and H. Reichl, "Troubleshooting and fixing of inverter driven induction motor bearing currents in existing plants of large size an evaluation of possible mitigation techniques in practical applications," in *Proc. IEEE APEC*, 2006, pp. 225–230.
- [32] R. Naik, T. Nondahl, M. Melfi, R. Schiferl, and J. Wang, "Shaft voltage prediction in induction motors fed by PWM ac drives," *IEEE Trans. Ind. Appl.*, vol. 39, no. 5, pp. 1294–1300, Sep./Oct. 2003.
- [33] *HewlettPackard/Agilent Model HP4284A LCR Meter, 20 Hz–1 MHz*. [Online]. Available: www.agilent.com
- [34] *AP Instruments Model 200 Analog Network Analyzer, 0.01 Hz–15 MHz*, p. 95 492, Windsor, CA. [Online]. Available: www.apinstruments.com
- [35] D. Maky, D. Novotny, and C. Thompson, "The influence of winding capacitance on high frequency time harmonic losses in Induction motors," in *Conf. Rec. IEEE IAS Annu. Meeting*, Oct. 1992, p. 33.
- [36] *IEEE Standard Test Procedure for Polyphase Induction Motors and Generators*, IEEE Standard 112, 1991.
- [37] G. Suresh, H. A. Toliyat, D. A. Rendusara, and P. N. Enjeti, "Predicting the transient effects of PWM voltage waveform on the stator windings of random wound induction motors," *IEEE Trans. Power Electron.*, vol. 14, no. 1, pp. 23–30, Jan. 1999.
- [38] D. Busse, J. Erdman, R. J. Kerkman, D. Schlegel, and G. Skibinski, "System electrical parameters and their effects on bearing currents," *IEEE Trans. Ind. Appl.*, vol. 33, no. 2, pp. 577–584, Mar./Apr. 1997.



Behrooz Mirafzal (S'01–M'05) received the B.Sc. degree in electrical engineering from Isfahan University of Technology, Isfahan, Iran, in 1994, the M.Sc. degree (with first class honors) in electrical engineering from the University of Mazandaran, Mazandaran, Iran, in 1997, and the Ph.D. degree in electrical engineering from Marquette University, Milwaukee, WI, in 2005.

From 1997 to 2000, he was a Research Engineer and a Lecturer with several academic institutions in Isfahan, Iran. Since 2005, he has been a Senior Development Engineer with the Motion Group, Rockwell Automation/Allen–Bradley, Mequon, WI. He has published 20 articles in professional journals and conference proceedings. He is the holder of one U.S. patent. He is currently involved in research and development related to servo motor drive systems. His research interests include power electronic applications, motor drive systems, and fault diagnostics in electric machines and drives.

Dr. Mirafzal is a member of Sigma Xi and the Electric Machines Committee of the IEEE Industry Applications Society.



Gary L. Skibinski received the B.S.E.E. and M.S.E.E. degrees from the University of Wisconsin, Milwaukee, in 1976 and 1980, respectively, and the Ph.D. degree from the University of Wisconsin, Madison, in 1992.

From 1976 to 1980, he was an Electrical Engineer with Eaton Corporation, where he worked on naval nuclear power. From 1981 to 1985, he was a Senior Project Engineer with the Allen–Bradley Company, where his work concerned servo controllers. During the Ph.D. program, he was a Consultant in UPS and switch-mode power supply products with R.T.E. Corporation. He is currently an Engineering Consultant with the Allen–Bradley Company, Rockwell Automation, Inc., Mequon, WI. He has published over 80 articles in professional journals and conference proceedings with 18 receiving prize awards. He is the holder of 18 U.S. patents. His current interests include power semiconductors, power electronic applications, and high-frequency high-power converter circuits for ac drives.



Rangarajan M. Tallam (S'97–M'01–SM'07) received the B.Tech. degree in electrical engineering from the Indian Institute of Technology, Madras, India, in 1997, and the M.S.E.E. and Ph.D. degrees in electrical engineering from the Georgia Institute of Technology (Georgia Tech), Atlanta, in 1999 and 2001, respectively.

From 2001 to 2005, he was a Senior Research Engineer with the Advanced Technology Division, Rockwell Automation, Milwaukee, WI, where he conducted research on active rectifiers and multilevel converters. He is currently a Senior Project Engineer with the Standard Drives Development Group, Rockwell Automation, Mequon, WI. He is the holder of two U.S. patents. His research interests are in switching power converter technology, motor control, and ac drive systems.

Dr. Tallam is a member of the IEEE Industry Applications, IEEE Power Electronics, and IEEE Industrial Electronics Societies.



Richard A. Lukaszewski (S'75–M'76–SM'04) received the B.S.E.E. degree from Milwaukee School of Engineering, Milwaukee, WI, in 1976, and the M.S. degree in engineering from the University of Wisconsin, Milwaukee, in 2004.

From 1976 to 1992, he was with Louis Allis/MagneTek, where he worked in drive systems engineering and later in drive development engineering, and on SCR-based current source inverters and bipolar and IGBT voltage source inverters. Since 1992, he has been with the Standard Drives Division,

Rockwell Automation, Mequon, WI, where he is currently a Program Manager. His team helped develop Rockwell Automation's flagship motor drive products from the 1336 generation to the present PowerFlex products. He is also the coauthor of several technical papers presented at IEEE Industry Applications Society (IAS) Conferences.

Mr. Lukaszewski has been a member of the IAS for 33 years and is currently a Senior Member. He is also involved with several committees within the IAS. He served in the Milwaukee Chapter of the IEEE IAS Section from 1980 to 1984. He was the Section Chairman of the Milwaukee Chapter when it won the "Best Large Chapter" Award presented at the 1984 IEEE IAS Annual Meeting in Chicago, IL. He was also the past Chair of the Power Devices and Components Committee (PEDCC) of the IAS. He currently serves as the Chair of the Industrial Power Conversion Systems Department (IPCS) of the IAS. He is also a Registered Professional Engineer in the State of Wisconsin.



David W. Schlegel (S'89–M'98) received the B.S.E.E.T. degree in electrical power engineering technology and the M.S.E. degree from the Milwaukee School of Engineering, Milwaukee, WI, in 1996 and 2001, respectively.

From 1979 to 2001, he was with Allen–Bradley, Rockwell Automation, where his last position was a Senior Development Engineer in advanced development. During this time, he made contributions to ac drive performance and the understanding of drive application issues. From 2001 to 2005, he was with ABB Inc., New Berlin, WI, where he was a Senior Development Engineer in R&D. While at ABB, he made contributions to the ASC550 drive development. Since 2005, he has been a Project Engineer in continuing engineering with Allen–Bradley, Rockwell Automation, Mequon, WI. He is responsible for 1336 and PowerFlex adjustable-speed drive product line engineering. His current interests include the modeling of ac drive system components, mitigation of application issues, and enhancing/maintaining drive performance.